The shape of the mitral annulus: A hypothesis of mechanical morphogenesis

Davide Ambrosi (iD)
DISMA, Politecnico di Torino, Torino, Italy

Luca Deorsola
Pediatric Cardiac Surgery Department, Ospedale Infantile Regina Margherita, Turin, Italy

Stefano Turzi
Dipartimento di Matematica, Politecnico di Milano, Milano, Italy

Marta Zoppello
DISMA, Politecnico di Torino, Torino, Italy

Abstract

This paper investigates the role of mechanics in the morphogenesis of the annulus of the mitral valve. We represent the annulus in its embryonic stage as an elastic ring and we perform a mechanical simulation of the development process applying a distributed torque on the rod: because of the mechanical action of the other growing cardiac chambers on the atrio-ventricular region, it departs from a planar circular shape. The numerical integration of the mathematical rod model subject to a bending load yields a shape very near to the one reported in the medical literature as anatomical reference for healthy patients. To make the comparison quantitative, we illustrate a numerical approach to match two curves in 3D defining their distance in a proper mathematical way. Such a methodology is first applied to compare the annular shape resulting from the mechanical model with an anatomical reference "master" shape and it is then applied to set to clinical data extracted from MRI for a cohort of healthy patients. The good agreement among anatomical master description, numerical mechanical model, and clinical data supports our speculation about a possible role of mechanics in determining the shape of the mitral valve.

1. Introduction

The cardiac valve which connects the left atrium to the left ventricle is known as Mitral Valve and allows blood to flow from the first cardiac chamber into the latter one, but not vice-versa. Even though this valve has a quite complex architecture, it can be essentially described as a structure formed by three components: the annulus, the

Corresponding author:
Davide Ambrosi, DISMA, Politecnico di Torino, Corso Duca degli Abruzzi 24, 10129 Torino, Italy.
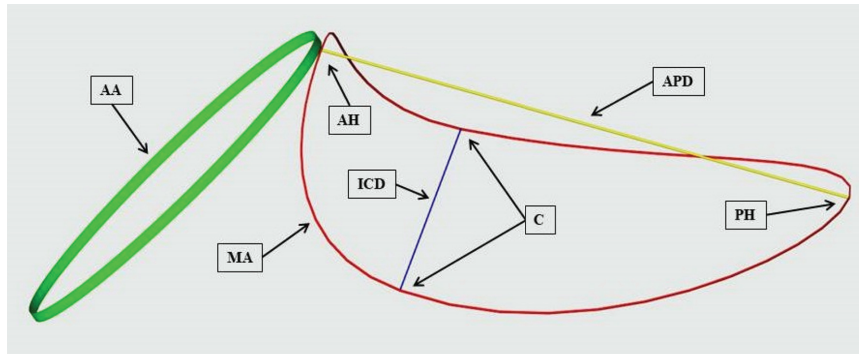Email: davide.ambrosi@polito.it

Figure 1. Sketch of the main geometrical features of the mitral annulus (red line) in contact with the aortic valve (green line). AA: aortica annulus; MA: mitral annulus; AH: anterior horn; PH: posterior horn; APD: anteroposterior diameter; C: commissures; ICD: intercommissural diameter.
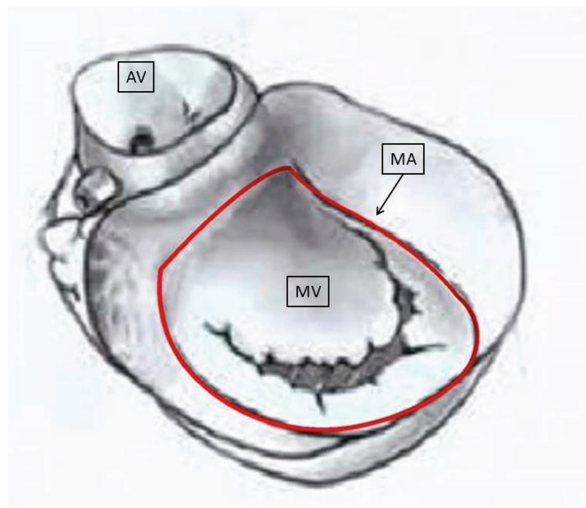

Figure 2. The stiffer aortic valve loads the softer mitral annulus that departs from its planar circular shape. MV: mitral valve; AV: aortic valve; MA: mitral annulus.

leaflets, and the subvalvular apparatus [1, 2]. The annulus is a ring with a specific three-dimensional geometry: it exhibits a peculiar saddle shape, which is widely described in the literature [1, 3–7].

The symmetric configuration of the valve ring allows us to identify two upper points and two lower ones (see Figure 1). The first upper point is located in the middle of the anterior annulus, close to the Aortic valve, while the second one is placed on the opposite side, in the middle of the posterior annulus. These two points are called *horns* and the line connecting them, which is known as *anteroposterior diameter*, divides the valve annulus into two specular halves. Conversely, the two lower points of the annular perimeter are located sideways, at the level of the two valve commissures, which can be geometrically defined as the points with maximum distance from the symmetry axis. Even though the overall shape might appear quite complex, at a closer look it can be effectively described as a circle bent upward at the level of the intercommissural diameter (see Figure 2).

Describing the valve annulus as a circle partially bent upward naturally leads to speculate about a possible explanation for the origin of its saddle shape during the embryonic heart development of the aortic valve [8–10].

To understand the mitral annular shape and its spatial relationship with the aortic valve, it is convenient to consider the most significant steps of the embryological cardiac development. Schematically speaking, we can identify eight main steps:

1. Originally, the heart develops as a tube, with two valves located at its ends: a common inlet valve and a common outlet valve (Figure 3(a)).
2. The tube bends assuming a U shape, and the lower end is displaced upper, thus positioning the two valves onto the same plane (Figure 3(b)).

3. The two vertical branches of the U-shaped cardiac tube fuse together, creating a common cardiac sac: a structure which is going to divide again into two separate parts, one on the left and one on the right, creating the two cardiac ventricles. The two common valves are now both located within the base of the sac, which is commonly called cardiac base (Figure 3(c)).
4. Each common valve starts to subdivide into two separate components: the common inlet valve gives birth to the mitral and the tricuspid components, while the outlet common valve to the aortic and the pulmonary components (Figure 3(d)).
5. The common valve subdivision is now complete and within the base of the cardiac sac there are four valves: two inlets and two outlets. The inlet valves are represented by the mitral valve, on the left, and the tricuspid valve, on the right. Since the mitral valve will be the inlet of the left ventricle and the tricuspid valve the inlet of the right one, their location appears correct within the cardiac base. On the contrary, the positions of the aortic and the pulmonary valves result inverted, being the first the outlet of the left ventricle and the latter the outlet of the right one (Figure 3(e)).
6. To generate a correct connection between the two outlet valves and the two halves of the cardiac sac, which has already started to subdivide into the two cardiac ventricles, the two outlet valves undergo a 90 degrees clockwise rotation, which moves the aortic valve posteriorly and the pulmonary valve anteriorly (Figure 3(f)).
7. When the rotation is complete, the aortic valve occupies a characteristic position, located in the center of the cardiac base and wedged between the mitral and the tricuspid valves. Until this stage, the four cardiac valves are almost circular and lie on the same plane. Anyway, the aortic valve motion is not completed yet: the mitral valve keeps on shifting posteriorly and towards the left side of the cardiac base, pushing the anterior annulus of the mitral valve (Figure 3(g)).
8. As a result of such a migration, the mitral and the aortic valves exit the common former plane: they both bank and rise their common contact point, like the pitches of a roof. While the stiff aortic valve preserves a circular and planar shape, the softer mitral valve bends, taking its characteristic saddle shape (Figure 3(h) and (i)).

The existence of this morphogenetic mechanism is indirectly supported by the biomedical literature: it is reported that congenital malformations generating an incomplete rotation and no displacement, as described in the items above, yield a pathological planar and circular mitral valve [11, 12].

We show in this paper that a load of the aortic annulus modeled as an elastic ring can mechanically provide a deformation of the mitral annulus yielding a shape very similar to the one observed in nature. The curve generated by numerical simulation of rod bending is qualitatively very similar to the anatomical description. To make the comparison quantitative, we have elaborated a numerical algorithm based on the *Procustes* method that measures in a least squares sense the distance between two closed curves described by an arbitrary number of points with any orientation and scaling of the axis. A similar question has been addressed in Cong et al. [13] with a different approach: the geometrical characteristics of an annulus are stated on the basis of a number of standard geometrical quantities as area, circumference, anteroposterior diameter, commissural width, and height. These geometrical indicators are usually compared with ranges obtained from clinical practice. Conversely, in this work, we address the *global* geometrical shape of an annulus represented by a set of points with coordinates captured by echocardiography, in terms of distance between two curves. The shape of the mitral valve annulus, represented as a curve in 3D, is compared both versus a reference anatomical one and versus the results of mechanical simulations supported by developmental arguments.

2. Rod model

In this section, the mitral annulus is mechanically represented as an inextensible and unshearable circular rod (a ring) subject to external forces and torques for a portion of its length. The external load accounts for the mechanical action of the adjacent growing chambers that bends the annulus, thus departing from the circular planar shape.

2.1. Kinematics

The centerline of our rod is a smooth curve $\mathbf{r}(s) : [0, L] \to \mathbb{R}^3$ parameterized by the arc length, in such a way that the vector tangent to the curve

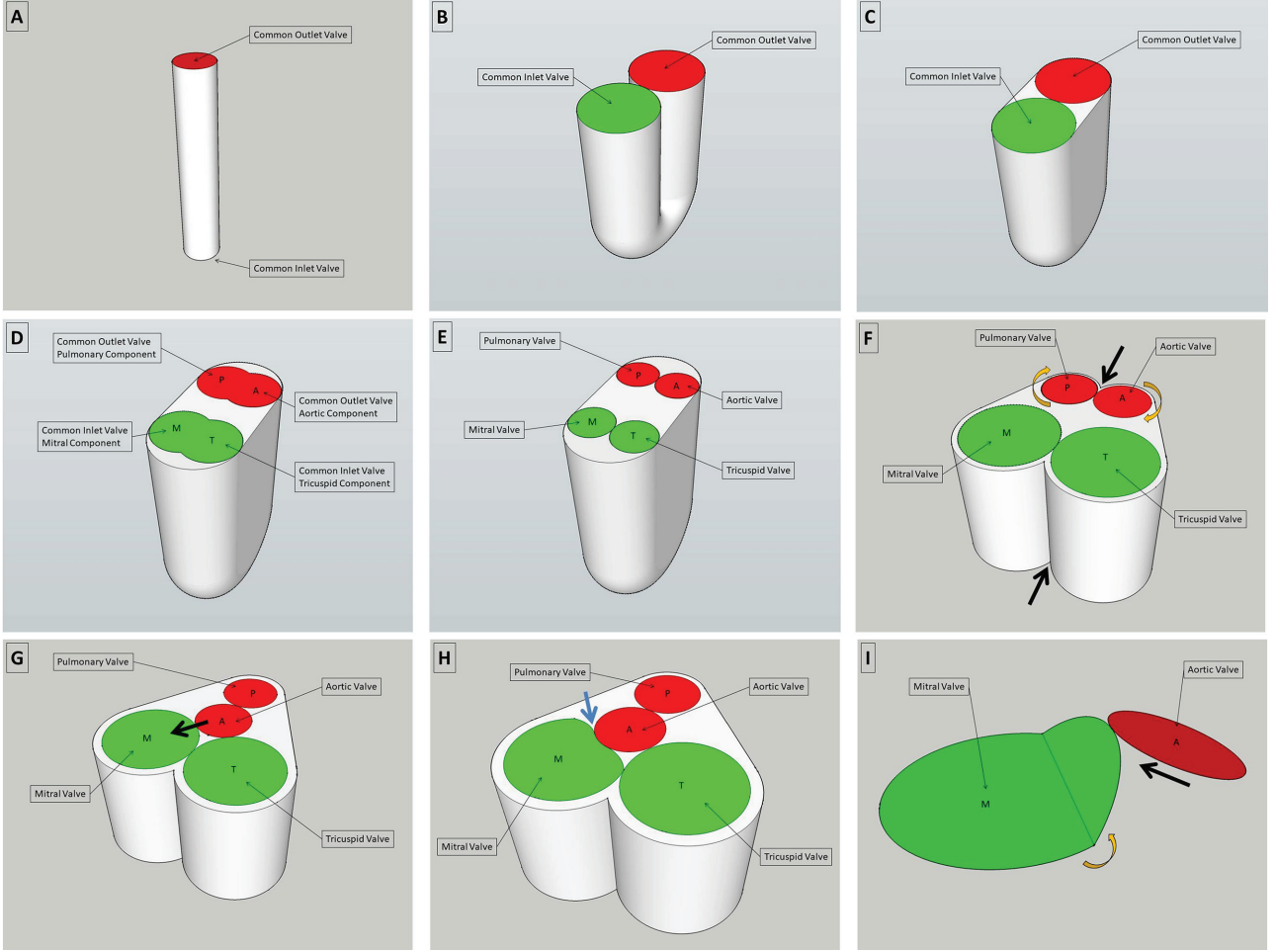$$d\mathbf{r}/ds = \mathbf{d}_1(s) \tag{1}$$

Figure 3. Sketch of the cardiac morphogenesis. The primordial cardiac tube bends and the separating wall is resorbed, then the original cardiac ends split into two valves that shift and rotate in a plane. When the mitral valve gets in contact with the aortic valve, they both exit from the plane and the former bends thus achieving the characteristic saddle shape.

is a unit vector. We associate to $\mathbf{d}_1$ other two orthogonal material unit vectors $\mathbf{d}_2(s), \mathbf{d}_3(s)$, linked to the material properties of the cross section of the rod, so that $\mathbf{d}_1(s), \mathbf{d}_2(s), \mathbf{d}_3(s)$ define a local orthonormal right-handed basis [14]. In the special case that $\mathbf{d}_2$ is parallel to $d\mathbf{d}_1/ds$, we recover the Frénet basis and $\mathbf{d}_3$ is the binormal vector. However, we do not assume such a special orientation in the following.

The unit vectors of the local basis satisfy

$$\frac{d}{ds}(\mathbf{d}_1 \cdot \mathbf{d}_1) = \frac{d}{ds}1 = 0 = 2\mathbf{d}_1' \cdot \mathbf{d}_1 \tag{2}$$

and so on, where we denote $\mathbf{d}_1' = d\mathbf{d}_1/ds$.

It follows that

$$\begin{aligned}
\mathbf{d}_1' &= (\mathbf{d}_1' \cdot \mathbf{d}_1)\mathbf{d}_1 + (\mathbf{d}_1' \cdot \mathbf{d}_2)\mathbf{d}_2 + (\mathbf{d}_1' \cdot \mathbf{d}_3)\mathbf{d}_3 = k_3\mathbf{d}_2 - k_2\mathbf{d}_3, \\
\mathbf{d}_2' &= (\mathbf{d}_2' \cdot \mathbf{d}_1)\mathbf{d}_1 + (\mathbf{d}_2' \cdot \mathbf{d}_2)\mathbf{d}_2 + (\mathbf{d}_2' \cdot \mathbf{d}_3)\mathbf{d}_3 = -k_3\mathbf{d}_1 + k_1\mathbf{d}_3, \\
\mathbf{d}_3' &= (\mathbf{d}_3' \cdot \mathbf{d}_1)\mathbf{d}_1 + (\mathbf{d}_3' \cdot \mathbf{d}_2)\mathbf{d}_2 + (\mathbf{d}_3' \cdot \mathbf{d}_3)\mathbf{d}_3 = k_2\mathbf{d}_1 - k_1\mathbf{d}_2,
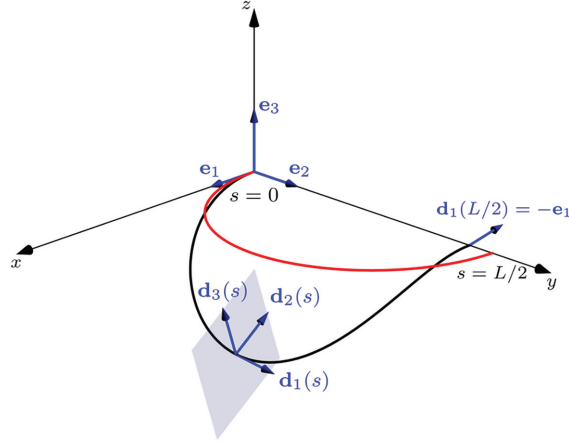\end{aligned} \tag{3}$$

Figure 4. The circular unloaded configuration of the mitral annulus (black) and the deformed one (red).

where $k_1(s), k_2(s), k_3(s)$ describe the rotation rate of the unit vectors of the local basis $(\mathbf{d}_1, \mathbf{d}_2, \mathbf{d}_3)$ moving along the curve. For the Frénet basis, $k_2 = 0$, k_3 is the centerline curvature, and k_1 is the torsion. In matrix form,

$$\begin{pmatrix} \mathbf{d}_1' \\ \mathbf{d}_2' \\ \mathbf{d}_3' \end{pmatrix} = \begin{pmatrix} 0 & k_3 & -k_2 \\ -k_3 & 0 & k_1 \\ k_2 & -k_1 & 0 \end{pmatrix} \begin{pmatrix} \mathbf{d}_1 \\ \mathbf{d}_2 \\ \mathbf{d}_3 \end{pmatrix} = \boldsymbol{\Omega} \begin{pmatrix} \mathbf{d}_1 \\ \mathbf{d}_2 \\ \mathbf{d}_3 \end{pmatrix} \tag{4}$$

where the skew–symmetric $\boldsymbol{\Omega}$ at the right-hand side represents the infinitesimal rotation of the basis. It can be rewritten as the product of two matrices

$$\boldsymbol{\Omega} = \mathbf{R}' \mathbf{R}^T \tag{5}$$

where $\mathbf{R}(s)$ is the finite rotation that brings the coordinate basis $(\mathbf{e}_1, \mathbf{e}_2, \mathbf{e}_3)$ into the current frame at position s: $\mathbf{d}_i(s) = \mathbf{R}(s)\mathbf{d}_i(0) = \mathbf{R}(s)\mathbf{e}_i$, $i = 1, 2, 3$ [15] (see Figure 4). The symbol ^{T} denotes transposition.

Summarizing: if the rotation rates (k_1, k_2, k_3) are known, given a suitable initial condition, the current basis $(\mathbf{d}_1(s), \mathbf{d}_2(s), \mathbf{d}_3(s))$ can be obtained by numerical integration of equation (4) and integration of equation (1) yields the actual configuration of the curve $\mathbf{r}(s)$. As a matter of fact, the force and momentum balance equations to be introduced in the next section are written in terms of the k_is.

2.2. Elastic energy and balance equations

An inextensible and unshearable slender body is here represented by a rod: a one-dimensional manifold embedded in the three-dimensional space. The deformation of a rod can be defined as the superposition of three independent motions: bending in two (local) planes and twist of the rod along its own direction.

Bending along three axis is kinematically represented by the curvature, the derivative of the tangent vector $\mathbf{d}_1'(s)$. For a planar deformation, this quantity is the inverse of the radius of the disc locally tangent to the rod: the more rapidly $\mathbf{d}_1$ changes direction versus the curvilinear coordinate, the larger is the curvature. In terms of infinitesimal rotation $\boldsymbol{\Omega}$, we define the squared curvature of a rod that is in its relaxed state in the reference configuration as $\kappa^2 = |\mathbf{d}_1'|^2 = k_2^2 + k_3^2$. The reference configuration might not be the relaxed one, as in the case of our interest, and natural bending and twist are to be included in the energetic description.

The twist of the beam is represented by the rotation of a vector normal to the rod (say $\mathbf{d}_3$) around the direction of the rod itself: in this case, $\tau^2 = |\mathbf{d}_3'|^2 - (\mathbf{d}_3' \cdot \mathbf{d}_1)^2 = k_1^2$, where the component of $\mathbf{d}_3'$ along $\mathbf{d}_1$ is not considered since it gives no contribution to the twist [16].

We assume that the elastic energy of the rod depends quadratically on its total curvature and twist obtained by integration along the curve:

$$W = \int_0^L \frac{\alpha}{2}(k_2 - k_{2o})^2 \, ds + \int_0^L \frac{\alpha}{2}(k_3 - k_{3o})^2 \, ds + \int_0^L \frac{\beta}{2}(k_1 - k_{1o})^2 \, ds \tag{6}$$

where k_{1o}, k_{2o} and k_{3o} are the natural twist and bending curvatures, respectively: the curvatures and twist that the rod owns in its own relaxed configuration (possibly different from the reference one). The bending modulus α and the twist modulus β depend on the material and geometrical characteristics of the rod as follows:

$$\alpha = EI, \qquad \beta = GJ, \tag{7}$$

where E is the Young modulus of the material, G is the shear modulus, I is the moment of inertia of the rod, and J is the axial moment. For the circular section, we consider $J = 2I$, while the assumption of incompressibility yields $G = E/3$ [17], so that eventually $\beta = \frac{2}{3}\alpha$.

The left-hand side of equation (6) can be rewritten in terms of the directors $\mathbf{d}_1$ and $\mathbf{d}_3$ using equations (3). Taking $k_{1o} = 0$, we consider a planar circle as reference relaxed configuration and we get

$$W = \int_0^L \frac{\alpha}{2}(k_2 - k_{2o})^2\, ds + \int_0^L \frac{\alpha}{2}(k_3 - k_{3o})^2\, ds + \int_0^L \frac{\beta}{2}k_1^2\, ds \tag{8}$$

$$= \int_0^L \frac{\alpha}{2}(-\mathbf{d}_1' \cdot \mathbf{d}_3 - k_{2o})^2 ds + \int_0^L \frac{\alpha}{2}(\mathbf{d}_1' \cdot \mathbf{d}_2 - k_{3o})^2 ds + \int_0^L \frac{\beta}{2}(\mathbf{d}_2 \cdot \mathbf{d}_3')^2 ds.$$

Before proceeding with calculations, we notice that for variations of the basis $(\mathbf{d}_1, \mathbf{d}_2, \mathbf{d}_3)$, the incremental directors should remain mutually orthonormal and therefore the admissible variations of the basis are of the form

$$\begin{aligned}
\delta\mathbf{d}_1 &= \mathbf{d}_2\, \delta\eta_3 - \mathbf{d}_3\, \delta\eta_2, \\
\delta\mathbf{d}_2 &= \mathbf{d}_3\, \delta\eta_1 - \mathbf{d}_1\, \delta\eta_3, \\
\delta\mathbf{d}_3 &= \mathbf{d}_1\, \delta\eta_2 - \mathbf{d}_2\, \delta\eta_1,
\end{aligned} \tag{9}$$

where $\delta\eta_i$ are arbitrary non-dimensional coefficients [18]. The coefficients $\delta\eta_i, i = 1, 2, 3$ should not be confused with the non-null components of the skew-symmetric matrix $\boldsymbol{\Omega}$: the latter provides the rate of rotation of the directors as a function of the curvilinear coordinate, the former are arbitrary independent rotation of the directors that allow us to identify the differential equations ensuring stationarity of the energy functional.

After appending the inextensibility and unshearability constraint (1) to the energy, we can write the principle of virtual work

$$\delta\hat{W}(k_1, k_2, k_3, \mathbf{N}, \mathbf{r}) = \delta\left(W(k_1, k_2, k_3) - \int_0^L \mathbf{N} \cdot (\mathbf{r}' - \mathbf{d}_1) ds\right) \tag{10}$$

$$= \int_0^L \left(\mathbf{f} \cdot \delta\mathbf{r} + \sum_1^3 m_i \delta\eta_i\right) ds$$

where the Lagrange multiplier $\mathbf{N}(s)$ is the reaction force (the tension of the rod) to the constraint $\mathbf{r}' = \mathbf{d}_1$, $\mathbf{f}(s)$ and $\mathbf{m}(s) = (m_1, m_2, m_3)$ are the active force and torque linear densities externally applied to the rod, represented in spatial coordinates, and $\delta\eta_i, i = 1, 2, 3$ are the entries of the skew-symmetric matrix defining the admissible variations of the basis $(\mathbf{d}_1, \mathbf{d}_2, \mathbf{d}_3)$ in equation (9). One might notice that $\mathbf{N}$ and $\mathbf{m}$ have the same physical dimensions, upper and lowercase denoting reactive and active forces, respectively. The tension $\mathbf{N}$ is represented in its spatial form

$$\mathbf{N} = \sum_1^3 N_i \mathbf{d}_i. \tag{11}$$

After first variation of the energy W, we get

$$\delta W = \int_0^L \alpha(-\mathbf{d}_1' \cdot \mathbf{d}_3 - k_{2o})\delta(-\mathbf{d}_1' \cdot \mathbf{d}_3)ds + \int_0^L \alpha(\mathbf{d}_1' \cdot \mathbf{d}_2 - k_{3o})\delta(\mathbf{d}_1' \cdot \mathbf{d}_2)ds \tag{12}$$

$$+ \int_0^L \beta(\mathbf{d}_2' \cdot \mathbf{d}_3)\delta(\mathbf{d}_2' \cdot \mathbf{d}_3)ds.$$

Variation of products and integration by parts yields

$$\delta W = \int_0^L \alpha\left((-\mathbf{d}_1' \cdot \mathbf{d}_3 - k_{2o})\mathbf{d}_3\right)' \cdot \delta\mathbf{d}_1 \, ds - \int_0^L \alpha(-\mathbf{d}_1' \cdot \mathbf{d}_3 - k_{2o})\mathbf{d}_1' \cdot \delta\mathbf{d}_3 \tag{13}$$

$$- \int_0^L \alpha\left((\mathbf{d}_1' \cdot \mathbf{d}_2 - k_{3o})\mathbf{d}_2\right)' \cdot \delta\mathbf{d}_1 \, ds + \int_0^L \alpha(\mathbf{d}_1' \cdot \mathbf{d}_2 - k_{3o})\mathbf{d}_1' \cdot \delta\mathbf{d}_2 \, ds$$

$$- \int_0^L \beta((\mathbf{d}_2' \cdot \mathbf{d}_3)\mathbf{d}_3)' \cdot \delta\mathbf{d}_2 \, ds + \int_0^L \beta(\mathbf{d}_2' \cdot \mathbf{d}_3) \, \mathbf{d}_2' \cdot \delta\mathbf{d}_3 \, ds + \text{boundary terms.}$$

We rewrite equation (13) in terms of the components of the infinitesimal rotation matrix using equation (4):

$$\delta W = -\alpha \int_0^L ((-(k_3\mathbf{d}_2 - k_2\mathbf{d}_3) \cdot \mathbf{d}_3 - k_{2o})\mathbf{d}_3)' \cdot \delta\mathbf{d}_1 \, ds \tag{14}$$

$$- \alpha \int_0^L (-(k_3\mathbf{d}_2 - k_2\mathbf{d}_3) \cdot \mathbf{d}_3 - k_{2o})(k_3\mathbf{d}_2 - k_2\mathbf{d}_3) \cdot \delta\mathbf{d}_3 \, ds$$

$$- \alpha \int_0^L (((k_3\mathbf{d}_2 - k_2\mathbf{d}_3) \cdot \mathbf{d}_2 - k_{3o})\mathbf{d}_2)' \cdot \delta\mathbf{d}_1 \, ds$$

$$+ \alpha \int_0^L ((k_3\mathbf{d}_2 - k_2\mathbf{d}_3) \cdot \mathbf{d}_2 - k_{3o})(k_3\mathbf{d}_2 - k_2\mathbf{d}_3) \cdot \delta\mathbf{d}_2 \, ds$$

$$- \beta \int_0^L (((k_1\mathbf{d}_3 - k_3\mathbf{d}_1) \cdot \mathbf{d}_3)\mathbf{d}_3)' \cdot \delta\mathbf{d}_2 \, ds$$

$$+ \beta \int_0^L ((k_1\mathbf{d}_3 - k_3\mathbf{d}_1) \cdot \mathbf{d}_3)(k_1\mathbf{d}_3 - k_3\mathbf{d}_1) \cdot \delta\mathbf{d}_3 \, ds + \text{b.t.}$$

$$= \alpha \int_0^L ((k_2 - k_{2o})\mathbf{d}_3)' \cdot \delta\mathbf{d}_1 \, ds - \alpha \int_0^L (k_2 - k_{2o})(k_3\mathbf{d}_2 - k_2\mathbf{d}_3) \cdot \delta\mathbf{d}_3 \, ds$$

$$- \alpha \int_0^L ((k_3 - k_{3o})\mathbf{d}_2))' \cdot \delta\mathbf{d}_1 \, ds + \alpha \int_0^L (k_3 - k_{3o})(k_3\mathbf{d}_2 - k_2\mathbf{d}_3) \cdot \delta\mathbf{d}_2 \, ds$$

$$- \beta \int_0^L (k_1\mathbf{d}_3)' \cdot \delta\mathbf{d}_2 \, ds + \beta \int_0^L k_1(k_1\mathbf{d}_3 - k_3\mathbf{d}_1) \cdot \delta\mathbf{d}_3, \, ds + \text{b.t.}$$

Using now the admissible variations formula (9), after some algebraic manipulations we get

$$\delta W = \alpha \int_0^L (-k_2'\delta\eta_2 - k_1(k_2 - k_{2o})\delta\eta_3 + k_3(k_2 - k_{2o})\delta\eta_1 \tag{15}$$

$$- k_3'\delta\eta_3 + k_1(k_3 - k_{3o})\delta\eta_2 - k_2(k_3 - k_{3o})\delta\eta_1) \, ds$$

$$+ \beta \int_0^L \left(-k_1'\delta\eta_1 + k_1k_2\delta\eta_3 - k_3k_1\delta\eta_2\right) ds + \text{b.t.}$$

First variation and integration by parts of the inextensibility constraints in equation (10) yields

$$-\int_0^L \delta\mathbf{N} \cdot (\mathbf{r}' - \mathbf{d}_1) ds - \int_0^L \mathbf{N} \cdot \delta\mathbf{r}' ds + \int_0^L \mathbf{N} \cdot \delta\mathbf{d}_1 \, ds = \tag{16}$$

$$-\int_0^L \delta\mathbf{N} \cdot (\mathbf{r}' - \mathbf{d}_1) \, ds + \mathbf{N} \cdot \delta\mathbf{r}\Big|_0^L + \int_0^L \mathbf{N}' \cdot \delta\mathbf{r} \, ds + \int_0^L \mathbf{N} \cdot (-\mathbf{d}_2\delta\eta_3 + \mathbf{d}_3\delta\eta_2) \, ds,$$

where the notation $\mathbf{N}'$ denotes the Poisson derivation rule applied to the spatial vector $\mathbf{N}$ as obtained using equations (11) and (4).

As the arguments of the constrained energy $\hat{W}(k_1, k_2, k_3, \mathbf{N}, \mathbf{r})$ vary independently, equation (10) rewritten in terms of explicit first variation as in equations (15) and (16) can only hold if the following Euler–Lagrange equations apply

$$\mathbf{N}' = \mathbf{f}, \tag{17a}$$

$$\beta k_1' + \alpha(k_3 k_{2o} - k_2 k_{3o}) + m_1 = 0, \tag{17b}$$

$$\alpha k_2' - k_1 k_3(\alpha - \beta) + \alpha k_1 k_{3o} + m_2 + N_3 = 0, \tag{17c}$$

$$\alpha k_3' + k_1 k_2(\alpha - \beta) - \alpha k_1 k_{2o} + m_3 - N_2 = 0, \tag{17d}$$

$$(\mathbf{d}_1', \mathbf{d}_2', \mathbf{d}_3')^T = \mathbf{\Omega}\,(\mathbf{d}_1, \mathbf{d}_2, \mathbf{d}_3)^T, \tag{17e}$$

$$\mathbf{r}' = \mathbf{d}_1. \tag{17f}$$

Equations (17a)–(17d) denote balance of force, torque, and bending moment, respectively [19]. Equation (17e) accounts for the rotation of the local basis versus the curvilinear coordinate. Equation (17f) enforces the inextensibility and unshearability constraint. Balance equations are to be supplemented by 18 boundary conditions that naturally show up when applying the variational procedure: we detail them for the specific case of interest in this paper in the next section.

Remark 1. In the mechanical literature, the balance equations (17) are often directly introduced, without going through a lengthy variational derivation. However, in the presence of constraints, such as the inextensibility and unshearability constraints, we assume the derivation of the balance equations from a variational principle is, in our opinion, more transparent and physically motivated.

3. The mitral valve annulus as a loaded circular rod

We represent the mitral valve annulus as a circular rod of length L, with null residual elastic energy: the body is relaxed in its circular configuration. The natural twist is therefore $k_{1o} = 0$, while the natural bending curvatures are $k_{2o} = 0, k_{3o} = \mathbf{d}_1' \cdot \mathbf{d}_2 = |\mathbf{d}_1'| = (2\pi)/L$.

To solve equations (17), the differential system has to be complemented by a suitable set of boundary conditions. As the mitral annulus is a closed curve, continuity conditions can be defined on the boundary for all the fields. We chose a different strategy, based on the observation that the anterior–posterior segment defines an axis of symmetry for the valve. We therefore restrict our numerical model to half the length of the annulus, as shown in Figure 4. The annulus at rest is in the (x, y) plane and the posterior saddle horn is placed in the origin of the axis (see Figure 3). The following boundary conditions apply:

$$\mathbf{r}(0) = (0, 0, 0), \tag{18a}$$

$$\mathbf{d}_1(0) = (1, 0, 0), \quad \mathbf{d}_2(0) = (0, 1, 0), \quad \mathbf{d}_3(0) = (0, 0, 1), \tag{18b}$$

$$x(L/2) = 0, \quad z(L/2) = 0, \tag{18c}$$

$$\mathbf{d}_1(L/2) \cdot \mathbf{e}_1 = -1, \quad \mathbf{d}_1(L/2) \cdot \mathbf{e}_2 = 0. \tag{18d}$$

The conditions on the directors $\mathbf{d}_1(s)$, $\mathbf{d}_2(s)$, and $\mathbf{d}_3(s)$ are easily translated into conditions on the components of the rotation matrix $\mathbf{R}(s)$, since $\mathbf{d}_i(s) = R_{1i}\mathbf{e}_1 + R_{2i}\mathbf{e}_2 + R_{3i}\mathbf{e}_3$, $i = 1, 2, 3$, where R_{ij} are the components of the orthogonal matrix $\mathbf{R}$. We note that it is sufficient to fix two components of the vector $\mathbf{d}_1$ in $s = L/2$. The third component is automatically determined because of the dynamics enforced by equation (5): if $\mathbf{R}$ is orthogonal at $s = 0$, $\mathbf{R}(s)$ is orthogonal for every s. As a consequence, the columns of $\mathbf{R}$ are unit vectors for every value of the curvilinear coordinate and enforcing two components of $\mathbf{d}_1$ in $s = L/2$ is sufficient to provide information on the whole unit vector.

Two more boundary conditions are needed. A first additional boundary condition is obtained by observing that in $s = L/2$ the y coordinate of the boundary point is not fixed, and therefore, no reaction force applies in such a direction. In rotated coordinates, the condition reads:

$$\mathbf{N}(L/2) \cdot \mathbf{e}_2 = \mathbf{N} \cdot (R_{21}\mathbf{d}_1 + R_{22}\mathbf{d}_2 + R_{23}\mathbf{d}_3)\Big|_{s=L/2}$$

$$= N_1 R_{21} + N_2 R_{22} + N_3 R_{23}\Big|_{s=L/2} = 0. \tag{19}$$

Likewise, we do not fix the twist at $s = L/2$, so that the end of the rod is free to rotate about the direction $\mathbf{d}_1(L/2)$, and the reactive torque must have a vanishing component along such a direction: $\mathbf{M}(L/2) \cdot \mathbf{d}_1(L/2) = 0$. Since $\mathbf{d}_1(L/2) = -\mathbf{e}_1$, and given the constitutive law for the torque that derives from the energy (6), the second additional boundary condition simply reads

$$k_1(L/2) = 0. \tag{20}$$

To model external actions on the rod, we consider a torque density $\mathbf{m}(s)$ applied on the portion of the rod corresponding to the saddle, bounded by the commissures in Figure 1. It represents the load of the aortic valve that bends the annulus during development, thus departing from the circular shape, and accounts for the clockwise bending around the x axis produced by the impinging arterial valve. It is described mathematically as a Gaussian profile centered at $s = \frac{3}{8}L$, with small standard deviation $\sigma = 0.05\,L$,

$$\mathbf{m}(s) = -\frac{m_0\,L}{\sqrt{2\pi\sigma^2}}\mathrm{e}^{\frac{-(s-3/8L)^2}{2\sigma^2}}\mathbf{e}_1, \tag{21}$$

with m_0 an adjustable parameter that determines the magnitude of the external torque density.

Remark 2. While we are not aware of mechanical literature discussing the mechanical properties of the mitral annulus on an experimental basis, it is known from clinical data that it undergoes 23%–40% variation in circumference length between the systolic and diastolic configuration [20]. While this observation apparently suggests an assumption of extensibility, we have adopted an inextensibility constraint in our model. The argument for this assumption is that we do not apply any elongating force to the annulus: we only apply bending force and couple. It is well known that the energy needed to bend an elastic rod is much smaller than the one needed to

elongate it and therefore we assume that our mechanical loads do not generate any elongation in the rod, so that no elongation energy storage has to be included in the model.

Remark 3. In the same vein of the comment above, to our knowledge, it is not reported in the biomechanical literature if the mitral annulus relaxes residual stress when excised. It is not therefore known whether the saddle-type shape or the annular form could be generated by residual stress produced by an inhomogeneous growth. In other words, the autonomous placement of the excised and cut annulus in a fully unconstrained and unloaded setting could provide information about the inner (growth) or outer (loads) nature of the shaping of the annulus. The former should be modeled by a suitable definition of the reference natural bending and twist k_{1o}, k_{2o} and k_{3o}, possibly depending on the curvilinear coordinate s. The latter is described by external loads, in terms of forces and torques. In the large existing anatomical literature are reported several figures of excised mitral valves, laying on a flat surface [20–24]. Most of the pictures display a flat structure with a rather homogeneous curvature. On the basis of such a very qualitative observation, we have decided to include in our model a natural bending corresponding to a flat relaxed circle (a ring). On the other hand, we are aware that the main interest of those pictorial representations was not mechanical, but anatomical, and this issue requires much deeper investigation. We only mention that mathematical modeling of pre-stressed biological materials is nowadays a consolidated area and the way to modify the model in terms of additive prestress or multiplicative prestrain is a well-understood subject [25]. In this respect, an interplay between external loads and internal remodeling couples is very plausible and deserves further studies [26].

4. Compare shapes: the distance between two curves

The numerical integration of the mechanical morphogenetic model described in the previous section provides us with a curve, possibly described pointwise: an array of ordered positions. These results data extracted from echocardiography or CT scan of patients that are arrays of positions captured at different mutual distance, different placement of the origin of the axis, and different spatial orientation. In order to make a significant comparison between curves, we apply the Procustes Method [27] that we detail and tailor below for our purposes.

We initially format the clinical data by performing the following operations:

- Approximate every pointwise curve by a spline, so that we have a smooth representation of every curve whatever is the number of points used to define it;
- Calculate the center of mass of every curve and translate it into the origin of the axis;
- Calculate the length of each curve ℓ_i and re-parameterize it so that each one has unitary length.

At this step, two curves must be oriented in a suitable way to make the comparison significant. We have in principle devised three possible approaches to provide such an orientation. The former approach is to utilize the axes of symmetry drawn by the radiologist, who identifies the intercommissural and the anterior–posterior diameters that now read as the axis of symmetry of the patients' valve to be aligned as the ones of the master valve. We have discarded this approach as it is operator-dependent (mainly for pathological valves) and we have then considered the possibility to calculate numerically the axis of symmetry of the curve represented by the principal axis of inertia of the curve (ordered according to the eigenvalues). Unfortunately, this methodology amplifies the noise that is unavoidably involved in the manual capture of coordinates and the axis of symmetry, even in the case of healthy valves, can be poorly reproduced.

Our final methodological choice is to look for the orthogonal transformation (including both rotations and reflections) that minimizes the distance between the two curves. Formally, let $\hat{\mathbf{p}}(s)$ and $\mathbf{p}(s)$ be the unitary length parametric representations of the master and of the patient annulus as obtained at the end of the steps illustrated above. We look for the orthogonal matrix $\mathbf{Q}$ such that the L^2 distance between the curves

$$\hat{\mathcal{F}}(\mathbf{Q}) = \int\limits_0^1 (\hat{\mathbf{p}}(s) - \mathbf{Q}\mathbf{p}(s))^2 ds, \tag{22}$$

is minimum. In a discrete representation, this requirement corresponds to minimize

$$\mathcal{F}(\mathbf{Q}) = \sum_{j=1}^n (\hat{\mathbf{p}}_j - \mathbf{Q}\mathbf{p}_j)^2, \tag{23}$$

where $\hat{\mathbf{p}}_j = \hat{\mathbf{p}}(s_j), \mathbf{p}_j = \mathbf{p}(s_j)$. The n nodes $0 \le s_j \le 1$ are equally spaced and the orthogonal matrix Q is such that $\mathsf{Q}^T\mathsf{Q} = \mathsf{Q}\mathsf{Q}^T = \mathsf{I}$.

Standard derivation of the functional $\mathcal{F}(\mathsf{Q})$ yields the equation

$$\sum_{j=1}^{n}(\hat{\mathbf{p}}_j - \mathsf{Q}\mathbf{p}_j) \cdot \delta\mathsf{Q}\mathbf{p}_j = 0. \tag{24}$$

As equation (24) must hold for any increment matrix $\delta\mathsf{Q}$, without enforcing at first its orthogonality, after transposition we get

$$\sum_{j=1}^{n}(\hat{\mathbf{p}}_j\mathbf{p}_j^T - \mathsf{Q}\mathbf{p}_j\mathbf{p}_j^T) = 0. \tag{25}$$

When defining

$$\mathsf{A} = \sum_{j=1}^{n}\hat{\mathbf{p}}_j\mathbf{p}_j^T \qquad \mathsf{B} = \sum_{j=1}^{n}\mathbf{p}_j\mathbf{p}_j^T, \tag{26}$$

we eventually get the matrix equation $\mathsf{Q}\mathsf{B} = \mathsf{A}$ or

$$\mathsf{Q} = \mathsf{A}\mathsf{B}^{-1}. \tag{27}$$

To enforce the requirement that Q is an orthogonal matrix, we calculate the singular value decomposition of the right-hand side of equation (27)

$$\mathsf{A}\mathsf{B}^{-1} = \mathsf{V}\mathsf{S}\mathsf{U}^T, \tag{28}$$

where V and U are orthogonal and S is diagonal positive definite. The projection of $\mathsf{A}\mathsf{B}^{-1}$ on the space of the orthogonal matrices is therefore represented by $\mathsf{V}\mathsf{U}^T$ [28] and, finally, we define the squared shape distance

$$d = \frac{1}{n}\sqrt{\sum_{j=1}^{n}(\hat{\mathbf{p}}_j - \mathsf{V}\mathsf{U}^T\mathbf{p}_j)^2}. \tag{29}$$

The shape distance d is non-dimensional because both curves have unitary length.

Remark 4. In the present work, we are deliberately adopting a sloppy definition of curve when we claim the aim to compare two "curves": as a matter of fact we are interested in comparing the *support* of two curves. Two closed curves can be actually different while sharing the same support if they have a different parameterization, different orientation, or different initial points. The notion of distance inherent in equation (23) is independent of the parameterization because the unit length curves are subdivided into the same number of equal subintervals. However, equation (23) is meaningful only if curves are defined starting from the same spatial position and with the same orientation. This is the case for the present work: clinical and master points have all been captured starting from the anterior horn and moving in clockwise orientation looking at the annulus from the atrium into the ventricle. However, we mention that even in the case of non-homogeneous data, a meaningful definition can be recovered by a more expensive strategy, minimizing the functions $\mathcal{F}$ also among any possible starting point and any orientation of the curves, that is, minimizing among all possible parameterizations. This is nothing but an L^2 version of the Fréchet distance that is usually defined with the L^∞ norm [29].

5. Numerical results

Numerical integration of equations (17)–(17f) with boundary condition (18)–(20) has been addressed by the solver bvp5c of Matlab. We use α to set the unit of measure of the bending stiffness (i.e., we set $\alpha = 1$ in the code) and choose the axial stiffness $\beta = 2/3\alpha$. The distributed torque applied on the annulus is centered in

$s = \frac{3}{8}L$, as stated in equation (21), and has a magnitude m_0 which we will vary from $0\,\alpha/L^2$ to $5\,\alpha/L^2$ in the simulations.

Remark 5. The distributed torque adopted in equation (21) is the simplest load that can be applied to a mechanical system that is still so poorly understood. We modulate the magnitude of the torque to optimize the results of the numerical simulation versus digital data. A more realistic representation of the load produced by the arterial valve on the mitral annulus could be obtained by addressing a larger system, where the growth of the arterial valve is included. In such a framework, **m** would not be *external* to the annular system (and therefore to prescribe) but they would be *internal* to the aortic annulus-mitral annulus system (an unknown to be calculated). This represents a natural direction of development of the present work.

5.1. Mechanical versus anatomical shape

A comparison between the anatomical shape reported in clinical literature as canonical reference curve [2] and the shape obtained on the basis of the mechanical model illustrated in section 3 are reported in Figure 5 The curves are in very good agreement; the only appreciable difference is in the top portion of the saddle, which appears slightly more rounded from mechanical simulations than in the anatomical model. The quantitative comparison is also very good: the mean squared difference between the curves as defined in equation (29) is $d = 0.01026$. Such a numerical value has to be compared with the unit length of the curve, so it tells us that the average difference is about 1% the length.

The solution is robust versus the choice of the torque magnitude m_0 illustrated in section 3. The weak dependence of the result versus the choice of the parameter is certified by the plot in Figure 6: the L^2 difference between the numerical solution and the canonical shape designed by anatomists is plotted versus the torque magnitude m_0. Around the optimal value $m_0 = 4.04\,\alpha/L^2$ the function is quite flat, thus exhibiting a poor dependence of the solution on the estimated value; quantitatively speaking, around the optimal value we have

$$\frac{\Delta d}{d} \simeq c \frac{\Delta m}{m}, \tag{30}$$

where Δ denotes the difference between the nearest values on the axis around the minimum d and the corresponding m. The value $c \simeq 0.35 < 1$ indicates poor dependence of the output versus the input.

5.2. Master anatomical versus clinical shape

A comparison between the anatomical reference shape and data extracted from the CT scan for a single specific patient is reported in Figure 7. The curves are in qualitative good agreement, except for undulations of the patient curve, a noise that could be expected. The mean squared difference between the curves defined as in equation (29) is $d = 0.01576$ slightly larger than the mechanical-to-master comparison.

A more meaningful measure is obtained by performing the same comparison with an average clinical curve extracted from a cohort of healthy adult patients. We define an *average* clinical mitral valve curve summing up all the curve supports of 26 patients *after* their reparameterization to unit length, displacement, and optimal orientation. The mean quadratic distance between the average clinical curve and the master one is $d = 0.01476$ (see Figure 6). The averaging procedure smooths out the wiggles typically produced by the operator extracting the data from medical images (see Figure 8). This result tells us that the rod shape defined in the medical literature as a golden representative of the mitral valve annulus and the one obtained on the basis of mechanical loads can be considered an excellent representative of the real (average) valvular annulus.

6. Final remarks

In this paper, we have investigated a conjecture about the morphogenesis of the mitral valve annulus from a theoretical mechanics point of view. We speculate that the characteristic saddle shape of the annulus can be produced by the mechanical load applied by the aortic valve during the embryonic development. The mitral valve annulus is therefore mechanically represented as an elastic ring, a circular rod bent by an external load. We apply a distributed torque on the portion of contact annulus, to mimic with the least complexity the load produced by impinging aortic annulus. The good agreement between the shape predicted by the mechanical model and the master shape defined as standard in the anatomical literature supports our morphogenetic conjecture.
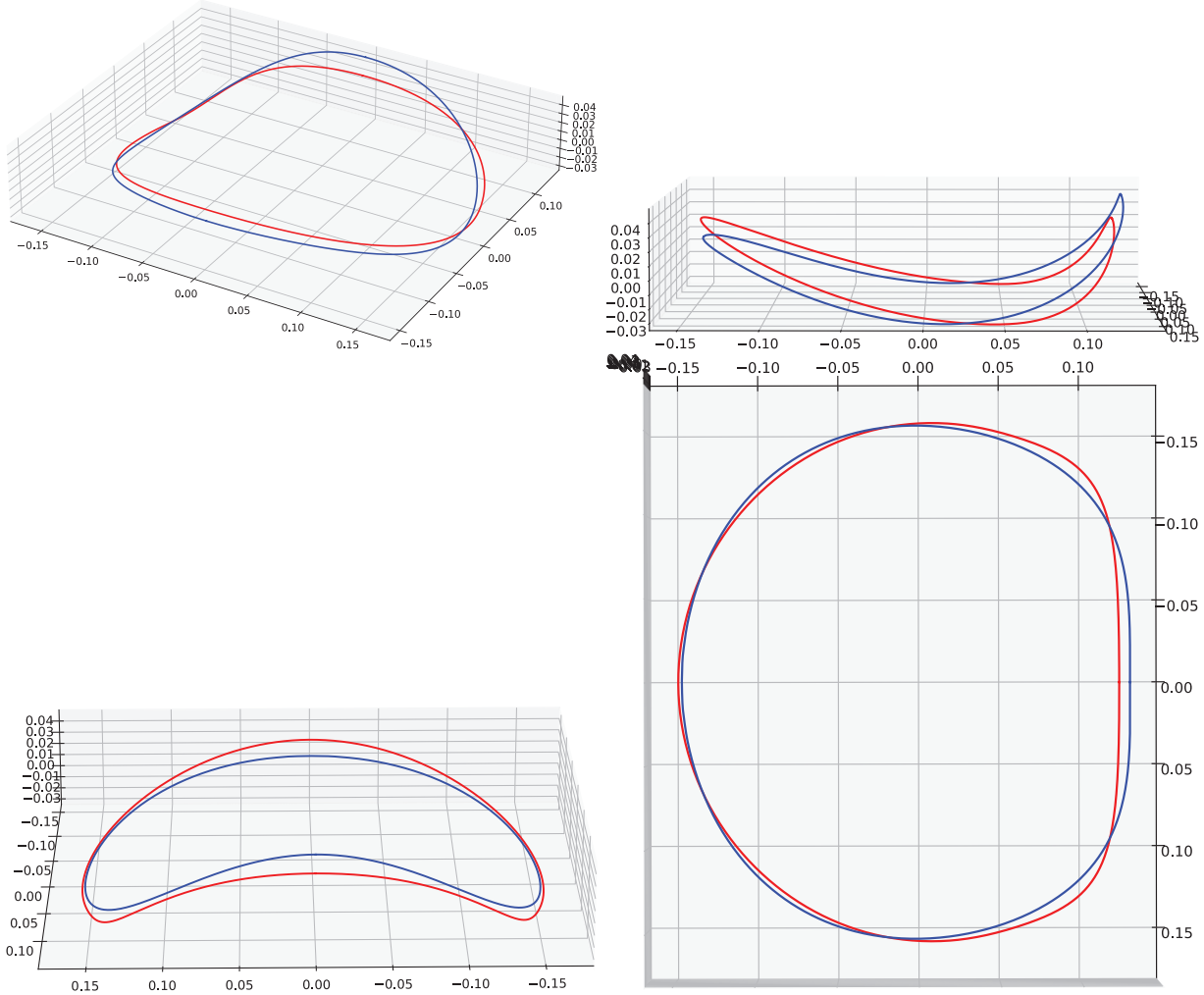
Figure 5. Several views of the curves representing the mitral annulus obtained by mechanical simulation (blue) and the one resulting from anatomical practice (red). The curves are in very good agreement except for the top portion of the saddle, which appears more rounded from mechanical simulations than in real anatomy.

The good reproduction of the saddle shape of the mitral annulus in terms of applied load is of course not a proof of concept that excludes other morphogenetic mechanisms: most likely the mechanical action of the aortic ring during development is accompanied by a development of the tissue that is partially shaped by the external mechanical stimuli. The extraction from data of this kind of information requires quite a sophisticated measure of residual stress of very soft matter, as in the case of arterial layers [30], and it has not yet been applied to the mitral annulus. The theoretical representation of growth and remodeling of living matter is however nowadays a well-understood subject [25], and we do not include this dynamics in the mathematical model only because of the lack of biomechanical information.

Our work is, to our knowledge, the first attempt to identify formally a role for mechanics in the mitral valve morphogenesis. Cardiac morphomechanics is still in its infancy and a limited number of studies have appeared in the mechanical literature (remarkable examples are [31] and [32]). The rod model adopted in the present work is a first step in the direction of a possible three-dimensional modeling of the mitral valve attached to the ventricle, thus introducing a more realistic mechanical interaction of the annulus with the surrounding tissue. In the same vein, experimental data are needed to support or falsify the assumption of relaxed plane circular shape that we have adopted here on the basis of extrapolation of medical images that had been captured for other aims.

Finally, a formal definition of the difference ("the distance") between two curves (their support, actually) has been needed to provide quantitative support to the comparison. To this aim, we have developed a numerical
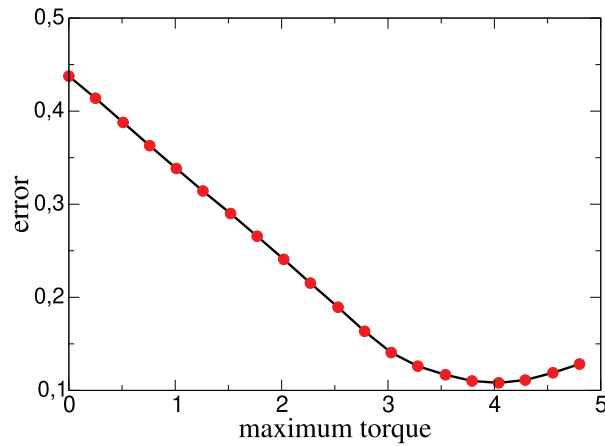
Figure 6. Plot of the difference between numerical and master curve (the "error") versus the maximum torque applied. The best fit of the data is obtained for $m_0 = 4.04\,\alpha/L^2$; however, the dependence of the result on the fitted parameter is weak, because the curve is quite flat around the minimum value.
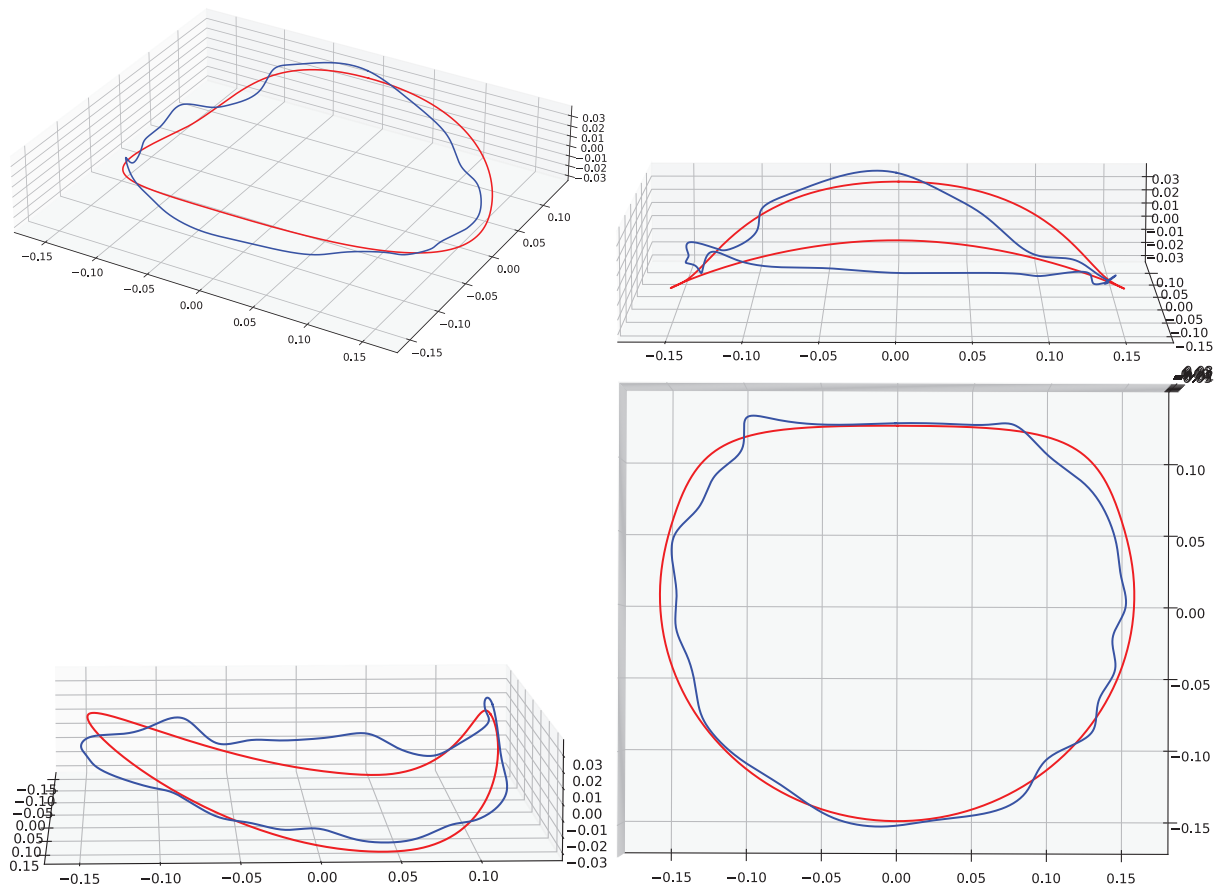

Figure 7. Side and top view of the curves representing the mitral annulus obtained by anatomical comparative studies (red) and one obtained by a single patient CT scan (blue). The curves are in very good agreement, the clinical one naturally exhibiting experimental noise.

method to compare in a precise mathematical sense the support of two closed curves, whatever their parameterization. The methodology is successfully applied to compare anatomical master description with results of the numerical mechanical model, single patient, and average clinical data. The effectiveness of the methodology suggests that our approach can be exploited in the future as a clinical tool to evaluate the degree of pathology
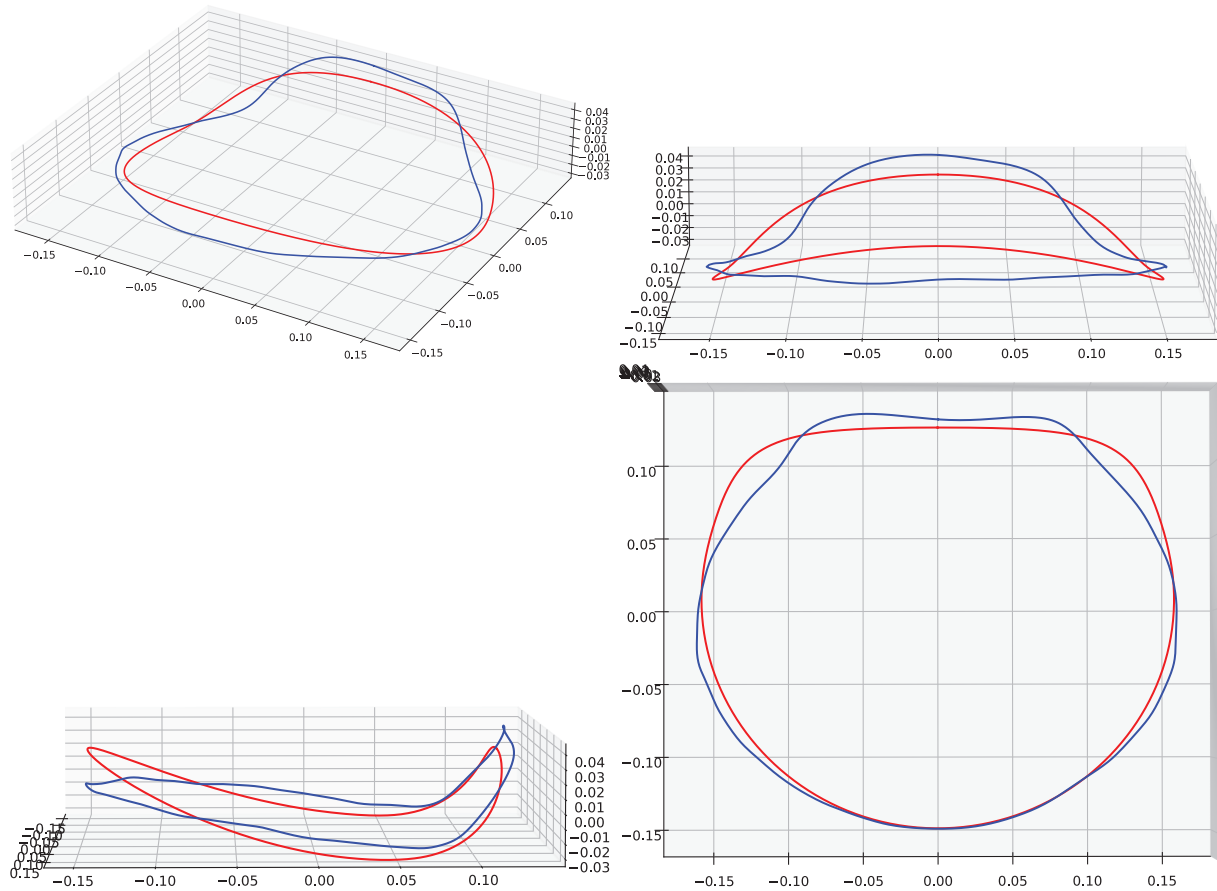
Figure 8. Several views of the curves representing the mitral annulus obtained by anatomical comparative studies (red) and the one obtained by average of a cohort of 26 patients CT scan (blue). The curves are in qualitative good agreement, the averaging procedure smooths out the operator-dependent wiggles.

of a mitral annulus: a large value of the shape distance d between a patient-specific annulus and the canonical healthy one, possibly encoded in a medical device, might automatically point out a pathological state to be further investigated.

Funding

ORCID iD

Davide Ambrosi https://orcid.org/0000-0003-2952-9613

References

[1] Oliveira, D, Srinivasan, J, Espino, D, et al. Geometric description for the anatomy of the mitral valve: a review. *J Anat* 2020; 237(2): 209–224.
[2] Deorsola, L, and Bellone, A. The golden proportion in the scallop geometry of normal mitral valves. when nature plays with jigsaw puzzles. *Echocardiography* 2019; 36(6): 1028–1034.
[3] Ryan, L, Jackson, B, Enomoto, Y, et al. Description of regional mitral annular nonplanarity in healthy human subjects: a novel methodology. *J Thorac Cardiovasc Surg* 2007; 134(3): 644–648.

[4]   Ryan, L, Jackson, B, Eperjesi, T, et al. Quantitative description of mitral valve geometry using real-time three-dimensional echocardiography. *Innovations* 2007; 2(5): 237–244.

[5]   Jolley, M, Ghelani, S, Adar, A, et al. Three-dimensional mitral valve morphology and age-related trends in children and young adults with structurally normal hearts using transthoracic echocardiography. *J Am Soc Echocardiogr* 2017; 30(6): 561–571.

[6]   Pouch, A, Vergnat, M, McGarvey, J, et al. Statistical assessment of normal mitral annular geometry using automated three-dimensional echocardiographic analysis. *Ann Thorac Surg* 2014; 97(1): 71–77.

[7]   Faletra, F, Leo, L, Paiocchi, V, et al. Anatomy of mitral annulus insights from non-invasive imaging techniques. *Eur Heart J Cardiovasc Imaging* 2019; 20(8): 843–857.

[8]   Restivo, A, Piacentini, G, Placidi, S, et al. Cardiac outflow tract: a review of some embryogenetic aspects of the conotruncal region of the heart. *Anat Rec A Discov Mol Cell Evol Biol* 2006; 288(9): 936–943.

[9]   Bajolle, F, Zaffran, S, Kelly, R, et al. Rotation of the myocardial wall of the outflow tract is implicated in the normal positioning of the great arteries. *Circulation research* 2006; 98(3): 421–428.

[10]   Goor, D, Dische, R, and Lillehei, C. The conotruncus: I. Its normal inversion and conus absorption. *Circulation* 1972; 46(2): 375–384.

[11]   Nam, H, Dinh, P, Lasso, A, et al. Dynamic annular modeling of the unrepaired complete atrioventricular canal annulus. *Ann Thorac Surg* 2022; 113(2): 654–662.

[12]   Kaza, E, Marx, G, Kaza, A, et al. Changes in left atrioventricular valve geometry after surgical repair of complete atrioventricular canal. *J Thorac Cardiovasc Surg* 2012; 143(5): 1117–1124.

[13]   Cong, T, Gu, J, Lee, A, et al. Quantitative analysis of mitral valve morphology in atrial functional mitral regurgitation using real-time 3-dimensional echocardiography atrial functional mitral regurgitation. *Cardiovasc Ultrasoun* 2018; 16(1): 1–10.

[14]   Goriely, A. Twisted elastic rings and the rediscoveries of Michell's instability. *J Elast* 2006; 84: 281–299.

[15]   Xavier, AJ. Static Kirchhoff rods under the action of external forces: integration via Runge-Kutta method. *J Comput Phys* 2014; 2014: 650365.

[16]   Bartels, S, and Reiter, P. Numerical solution of a bending-torsion model for elastic rods. *Numer Math* 2020; 146(4): 661–697.

[17]   Goriely, A, and Tabor, M. Nonlinear dynamics of filaments I. Dynamical instabilities. *Physica D* 1997; 105(1-3): 20–44.

[18]   Steigmann, D, and Faulkner, M. Variational theory for spatial rods. *J Elast* 1993; 33(1): 1–26.

[19]   Audoly, B, and Pomeau, Y. Elasticity and geometry. In: Kaiser, R (ed.) *Peyresq lectures on nonlinear phenomena*. Singapore: World Scientific, 2000, pp. 1–35.

[20]   van Rijk-Zwikker, G, Delemarre, B, and Huysmans, H. Mitral valve anatomy and morphology: relevance to mitral valve replacement and valve reconstruction. *J Card Surg* 1994; 9: 255–261.

[21]   Ho, S. Anatomy of the mitral valve. *Heart* 2002; 88(Suppl. 4): iv5–iv10.

[22]   Mishra, P, Rao, M, Paranjape, V, et al. Morphometry of mitral valve. *Med J DY Patil Univ* 2014; 7(5): 625.

[23]   Du Plessis, L, and Marchand, P. The anatomy of the mitral valve and its associated structures. *Thorax* 1964; 19(3): 221.

[24]   Muresian, H, Diena, M, Cerin, G, et al. The mitral valve: new insights into the clinical anatomy. *Maedica* 2006; 1: 80–87.

[25]   Taber, L. Biomechanics of growth, remodeling, and morphogenesis. *Appl Mech Rev* 1995; 48(8): 487–545.

[26]   Ambrosi, D, and Guana, F. Stress-modulated growth. *Math Mech Solids* 2007; 12(3): 319–342.

[27]   Arun, K, Huang, T, and Blostein, S. Least-squares fitting of two 3-D point sets. *IEEE Trans Pattern Anal Mach Intell* 1987; PAMI-9(5): 698–700.

[28]   Higham, N. Matrix nearness problems and applications. In: Gover, M, and Barnett, S (eds) *Applications of matrix theory*. Oxford: Oxford University Press, 1989, pp. 1–27.

[29]   Alt, H, and Godau, M. Computing the Fréchet distance between two polygonal curves. *Int J Comput Geom Appl* 1995; 5: 75–91.

[30]   Alford, P, Humphrey, J, and Taber, L. Growth and remodeling in a thick-walled artery model: effects of spatial variations in wall constituents. *Biomech Model Mechanobiol* 2008; 7: 245–262.

[31]   Ramasubramanian, A, Latacha, K, Benjamin, J, et al. Computational model for early cardiac looping. *Ann Biomed Eng* 2006; 34: 1355–1369.

[32]   Bevilacqua, G, Ciarletta, P, and Quarteroni, A. Morphomechanical model of the torsional c-looping in the embryonic heart. *SIAM J Appl Math* 2021; 81(3): 897–918.